# On the Dynamical Causes of Variability in the Rain-Shadow Effect: A Case Study of the Washington Cascades

NICHOLAS SILER

*Department of Atmospheric Sciences, University of Washington, Seattle, Washington*

GERARD ROE

*Department of Earth and Space Sciences, University of Washington, Seattle, Washington*

DALE DURRAN

*Department of Atmospheric Sciences, University of Washington, Seattle, Washington*

(Manuscript received 15 March 2012, in final form 13 August 2012)

ABSTRACT

Washington State's Cascade Mountains exhibit a strong orographic rain shadow, with much wetter western slopes than eastern slopes due to prevailing westerly flow during the winter storm season. There is significant interannual variability in the magnitude of this rain-shadow effect, however, which has important consequences for water resource management, especially where water is a critically limited resource east of the crest. Here the influence of the large-scale circulation on the Cascade rain shadow is investigated using observations from the Snowfall Telemetry (SNOTEL) monitoring network, supplemented by stream gauge measurements. Two orthogonal indices are introduced as a basis set for representing variability in wintertime Cascade precipitation. First, the total precipitation index is a measure of regionwide precipitation and explains the majority of the variance in wintertime precipitation everywhere. Second, the rain-shadow index is a measure of the east–west precipitation gradient. It explains up to 31% of the variance west and east of the crest. A significant correlation is found between the winter-mean rain shadow and ENSO, with weak (strong) rain shadows associated with El Niño (La Niña). The analysis is supported by streamflow data from eastern and western watersheds. A preliminary review of individual storms suggests that the strongest rain shadows are associated with warm-sector events, while the weakest rain shadows occur during warm-frontal passages. This is consistent with known changes in storm tracks associated with ENSO, and a variety of mechanisms likely contribute.

## 1. Introduction

One of the most distinctive features of mountain climates is the ''rain-shadow effect''—the sharp decline in precipitation often observed in the lee of mountain ranges. In the midlatitudes where prevailing winds are westerly, particularly strong rain shadows are associated with mountain ranges oriented north–south, such as the Sierra Nevada, the Cascades, the Southern Alps, and the southern Andes. In the lee of these ranges, annual precipitation is often an order of magnitude lower than at the wettest locations upstream of their crests, leading to significant ecological, hydrological, and economic differences between eastern and western slopes.

The basic physics of the rain-shadow effect is well known (e.g., Smith 1979; Roe 2005). On windward slopes, ascending air expands and cools; if the air is saturated, such ascent will force water vapor to condense, enhancing precipitation. In the lee precipitation is suppressed as descending air warms and extant liquid water evaporates. Despite this simple picture, however, the mechanisms controlling the strength of the rain shadow (i.e., the magnitude of the east–west precipitation gradient) remain poorly understood. With the exception of a few studies focused on extreme leeside precipitation events in the Sierra Nevada (e.g., Underwood et al. 2009; Kaplan et al. 2009) and the Southern Alps

*Corresponding author address:* Nicholas Siler, Department of Atmospheric Sciences, University of Washington, Box 351310, Seattle, WA 98195.
E-mail: siler@atmos.washington.edu

DOI: 10.1175/JHM-D-12-045.1

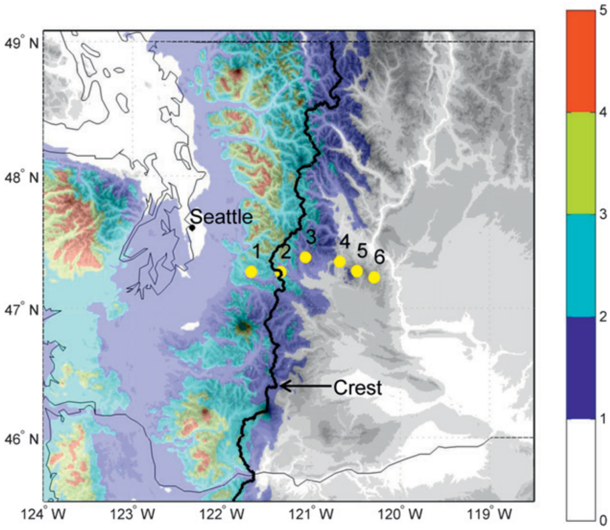


FIG. 1. Annual precipitation (color contours, m) and elevation (gray contours, 300-m intervals) over the Cascades. Yellow circles, numbered sequentially from west to east, mark the locations of SNOTEL stations included in the analysis. The SNOTEL stations are 1: Cougar Mountain, 2: Stampede Pass, 3: Sasse Ridge, 4: Blewett Pass, 5: Grouse Camp, and 6: Trough. Source of precipitation data is the Parameter-Elevation Regressions on Independent Slopes Model (PRISM) Climate Group, Oregon State University.

(e.g., Sinclair et al. 1997; Chater and Sturman 1998), there has been remarkably little research into what controls rain-shadow strength, especially on interannual time scales. Since the circulation is likely to change as the planet warms (e.g., Selten 2004; Yin 2005), it is important to understand the controlling processes of rain-shadow strength in more detail.

This paper represents a first step toward such an understanding, using the Cascades of Washington State as a case study. We have chosen to focus on the Cascades for two reasons. Firstly, the Cascade rain shadow is among the strongest in the world, with annual precipitation of more than 4 m on many western ridges and less than 25 cm in much of the Columbia River basin to the east (Fig. 1). Secondly, variability in the amount and distribution of Cascade precipitation can have important societal consequences. With a climate of cool, wet winters and warm, dry summers, the region derives much of its water supply from winter snowpack. During the summer dry season, snowmelt largely sustains the region's rivers and reservoirs, providing hydroelectric power, irrigation water, spawning habitat for salmon, and drinking water to several million people in the Puget Sound and Columbia basin regions. A dry winter can result in summer streamflows that are insufficient to meet society's needs, particularly in eastern watersheds like the Yakima, where irrigation has transformed a desert into the most productive agricultural region in the state. An unusually dry winter in 2000/01, for example, left the Yakima Valley with estimated crop losses of $100 million (Scott et al. 2004).

Like any climate variable, wintertime precipitation in the Cascades varies both in space and in time. On seasonal time scales, spatial variability is often assumed to be negligible, and a single time series is used for precipitation (or snowpack) over the entire Cascade range (e.g., Serreze et al. 1999; Mote et al. 1999; Hayes et al. 2002; Casola et al. 2009; Stoelinga et al. 2010; Smoliak et al. 2010). However, recent studies have shown that this assumption may be flawed, at least when applied to interannual variability in wintertime precipitation. For example, in an analysis of 51 years of gridded precipitation data interpolated from the Cooperative Observer (COOP) network, Leung et al. (2003) found that the impact of the El Niño–Southern Oscillation (ENSO) on wintertime precipitation differs east and west of the Cascade crest, with warm (El Niño) episodes bringing less precipitation to western Washington but more precipitation to eastern Washington, while cold (La Niña) episodes have the opposite effect. Others have found similar spatial variations in model forecasts of regional climate change, with some models projecting drier conditions for western slopes but wetter conditions for eastern slopes in future winters (Salathé et al. 2010; Zhang et al. 2011). These results imply that the spatial distribution of wintertime Cascade precipitation is not fixed and that the strength of the rain shadow, in particular, varies in response to natural and anthropogenic changes in the climate.

In this paper we present a new analysis of Cascade precipitation—one that seeks to understand variability not only in total precipitation but also in the strength of the rain shadow. Our analysis begins in section 3, where we demonstrate two orthogonal modes of variability in Cascade wintertime precipitation: one associated with total precipitation and the other with rain-shadow strength. We then identify the large-scale circulation patterns corresponding to each mode, finding that the rain-shadow pattern strongly resembles the ENSO teleconnection pattern. In section 4, we repeat the analysis for streamflow data, confirming that our results apply generally to the entire Washington Cascades. In section 5, we take a detailed look at individual storms exhibiting strong and weak rain shadows. We find that that a strong rain shadow is associated with warm-sector precipitation and a northern Pacific storm track, while a weak rain shadow is associated with warm-frontal precipitation and a southern storm track. Finally, we examine the dynamical reasons for these differences in the context of two case studies.

## 2. Data

Two datasets are used in our statistical analysis, and we present results for wintertime, here defined as December–February (DJF). We have chosen DJF partially out of convention (e.g., Horel and Wallace 1981; Yarnal and Diaz 1986; Robertson and Ghil 1999) but also because it represents the period of greatest snowpack accumulation, making it the most important period for determining summer streamflows (Serreze et al. 1999). Though not presented here, results for the water half-year (October–March) were found to be similar to the DJF results.

Our precipitation data come from six Snowfall Telemetry (SNOTEL) stations shown in Fig. 1, which constitute a roughly 100-km east–west transect through a central portion of the Cascades. Precipitation has been measured at each station since 1982, providing a continuous 28-yr time series of DJF precipitation. In this study we focus exclusively on this transect because of its relatively simple geometry and high station density. However, we separately analyzed other SNOTEL transects to the north and south and found essentially the same results. The generality of our results is further supported by river gauge data, as we discuss in section 4. Therefore, we are confident that these six SNOTEL stations accurately represent precipitation variability in the Washington Cascades as a whole.

Use of such a sparse dataset requires highly accurate data, and the seasonal SNOTEL precipitation data used in our analysis meet this criterion. According to the Natural Resources Conservation Service (NRCS), which maintains the SNOTEL network, the DJF precipitation totals at each site are currently accurate to within 0.5 inches, which is less than 5% of the mean at the driest site in the transect (J. Curtis, NRCS, 2011, personal communication). This level of accuracy is achieved by using snow pillow measurements to correct for rain gauge errors during freezing conditions when the gauges are susceptible to icing. While we cannot confirm that such a high level of accuracy has been maintained throughout the study period, we have no reason to suspect the existence of biases or errors large enough to significantly affect the results of our analysis.

For the large-scale atmospheric circulation we use monthly-averaged 500-hPa height fields from the European Centre for Medium-Range Weather Forecasts (ECMWF) Re-Analysis (ERA)-Interim data, gridded at 0.75° horizontal resolution (Dee et al. 2011). We chose the 500-hPa level in order to isolate the influence of the large-scale circulation, absent any topographic influence. However, the results that we present using 500-hPa heights are not substantially different than the results using 850-hPa heights or sea level pressure, particularly in the Pacific where topography plays no role.

TABLE 1. Correlation coefficients of DJF precipitation among the six SNOTEL stations shown in Fig. 1. The data span 28 seasons from 1982 to 2010. Stations are numbered in ascending order from west to east.

| | $P_1$ | $P_2$ | $P_3$ | $P_4$ | $P_5$ | $P_6$ |
|---|---|---|---|---|---|---|
| $P_1$ | * | | | | | |
| $P_2$ | 0.94 | * | | | | |
| $P_3$ | 0.88 | 0.91 | * | | | |
| $P_4$ | 0.84 | 0.85 | 0.93 | * | | |
| $P_5$ | 0.61 | 0.64 | 0.78 | 0.83 | * | |
| $P_6$ | 0.38 | 0.43 | 0.63 | 0.65 | 0.89 | * |

## 3. Statistical analysis

We begin with a statistical analysis of the 28-yr time series of wintertime precipitation at the six SNOTEL stations shown in Fig. 1, which constitute a representative cross section of the entire Washington Cascades. Because average precipitation is higher at the western end of the transect, the raw time series have substantial differences in both mean and variance. To compensate for this, we normalize each one by subtracting its mean and dividing by its standard deviation. None of the time series showed a significant trend over the 28-yr period. We have assigned each station a number from one to six, increasing from west to east, and refer to the normalized time series of wintertime precipitation at the $n$th station as $P_n$.

The Pearson correlation coefficients among the six SNOTEL stations are presented in Table 1. The correlations are uniformly positive, indicating that a wet (or dry) winter at one station also tends to be a wet (or dry) winter at the other stations. However, the correlations are remarkably weak between the stations at the opposite ends of the transect: $P_1$ and $P_6$ are correlated at just 0.38, which also turns out to be the threshold for statistical significance at the 95% confidence level. Thus, while it is clear that there is a statistically significant common signal, there must also be some substantial independent controls on windward and leeward precipitation. The circulation patterns responsible for the linear independence between $P_1$ and $P_6$ will be discussed in detail later in this section.

To more cleanly quantify the precipitation variability across the transect it is helpful to express the data in terms of a basis set with fewer dimensions. Techniques such as principal component analysis (PCA) are often used for this purpose, but we have chosen a different approach that we consider to be more intuitive (though

TABLE 2. Row 1: correlation coefficients between the time series of DJF precipitation at each SNOTEL station and its least squares projection onto $P_1$ and $P_6$. High correlations mean that $P_1$ and $P_6$ nearly span the vector space of the six time series. Rows 2 and 3: the weights of $P_1$ and $P_6$ that make up each time series.

| | $P_1$ | $P_2$ | $P_3$ | $P_4$ | $P_5$ | $P_6$ |
|---|---|---|---|---|---|---|
| Corr($P_n$, $P_n^*$) | 1 | 0.96 | 0.94 | 0.91 | 0.94 | 1 |
| $\alpha$ | 1 | 0.91 | 0.75 | 0.69 | 0.31 | 0 |
| $\beta$ | 0 | 0.08 | 0.35 | 0.38 | 0.76 | 1 |

TABLE 3. Row 1: the correlation coefficients between $R$ and the least squares approximation of normalized DJF precipitation at each SNOTEL station ($P_n^*$). Row 2: the fraction of variance in $P_n^*$ that is explained by $R$.

| | $P_1^*$ | $P_2^*$ | $P_3^*$ | $P_4^*$ | $P_5^*$ | $P_6^*$ |
|---|---|---|---|---|---|---|
| $r_R$ | 0.56 | 0.46 | 0.22 | 0.17 | −0.25 | −0.56 |
| $r_R^2$ | 0.31 | 0.21 | 0.05 | 0.03 | 0.06 | 0.31 |

the end result is essentially the same). To motivate our approach, we first note that each time series can be well characterized as a linear combination of $P_1$ and $P_6$:

$$P_n \approx P_n^* = \alpha_n P_1 + \beta_n P_6, \tag{1}$$

where the coefficients $\alpha_n$ and $\beta_n$ are determined by ordinary least squares regression. The effectiveness of this approximation is demonstrated in Table 2. The first row of numbers are the correlation coefficients between $P_n$ and $P_n^*$. All correlations exceed 0.90, which demonstrates that $P_1$ and $P_6$ alone span almost the whole vector space of the six time series. The relative weights of $P_1$ and $P_6$ in each time series are given in the last two rows of the table.

In light of this result, we construct a basis set consisting of two indices: a total precipitation index

$$T = P_1 + P_6, \tag{2}$$

and a rain-shadow index

$$R = P_1 - P_6. \tag{3}$$

Here $T$ is a measure of the common precipitation anomaly across the transect; it is highest when it is unusually wet everywhere. In contrast, $R$ measures the strength of the rain-shadow effect: high positive values indicate a stronger-than-average east–west precipitation gradient, while negative values indicate a weaker-than-average precipitation gradient.

A basis set consisting of $T$ and $R$ has the following useful properties.

(i) Like $P_1$ and $P_6$, $T$ and $R$ nearly span the vector space of precipitation along the transect. Each time series is well approximated as a linear combination of $T$ and $R$, and $T$ and $R$ explain 100% of the variance in each approximate time series $P_n^*$.

(ii) Because $P_1$ and $P_6$ have unit variance, $T$ and $R$ represent orthogonal modes of variability, and the variances explained by the two indices are independent of each other.

(iii) Unlike PCA, in which each principal component explains a certain fraction of variability over the entire domain, our basis allows us to evaluate the relative importance of $T$ and $R$ at each station along the transect. Rain-shadow variability is important wherever $R$ explains a substantial fraction of the variance in total precipitation.

As a measure of the importance of rain-shadow variability along the transect, we present the correlation coefficients between $R$ and $P_n^*$ in the first row of Table 3. Where the correlation coefficients switch from positive to negative (between sites 4 and 5) represents the fulcrum of the rain-shadow mode: west (east) of this point, a larger value of $R$ corresponds to above-average (below average) precipitation. Near the fulcrum (sites 3, 4, and 5), correlations with $R$ are relatively weak, indicating that precipitation variability at these locations is well characterized by $T$ alone.

Squaring these correlation coefficients, we find that $R$ explains, at most, 31% of the variance in $P^*$ along the transect, while $T$ accounts for the rest (second row of Table 3). We will return to this result in our watershed analysis in section 4. But first we explore the patterns of atmospheric circulation associated with both $T$ and $R$.

### *Atmospheric circulation patterns associated with T and R*

How does the large-scale atmospheric circulation contribute to fluctuations in $T$ and $R$? We first present covariance maps of the DJF 500-hPa height anomalies with the time series of $T$ and $R$ (Figs. 2a,b). For reference, we also include a map of the mean DJF 500-hPa heights between 1982 and 2010 (Fig. 2c), which shows a stationary wave pattern characterized by low-pressure troughs in the storm track regions of the northwest Pacific and Atlantic basins and a ridge over the west coast of North America.

The covariance maps (Figs. 2a,b) depict height anomalies associated with positive values of $T$ and $R$; when the indices are negative, the anomaly pattern is inverted. Because $T$ and $R$ are just the sum and difference of $P_1$ and $P_6$, these covariance maps are the same as would be created by regressing separately onto $P_1$ and

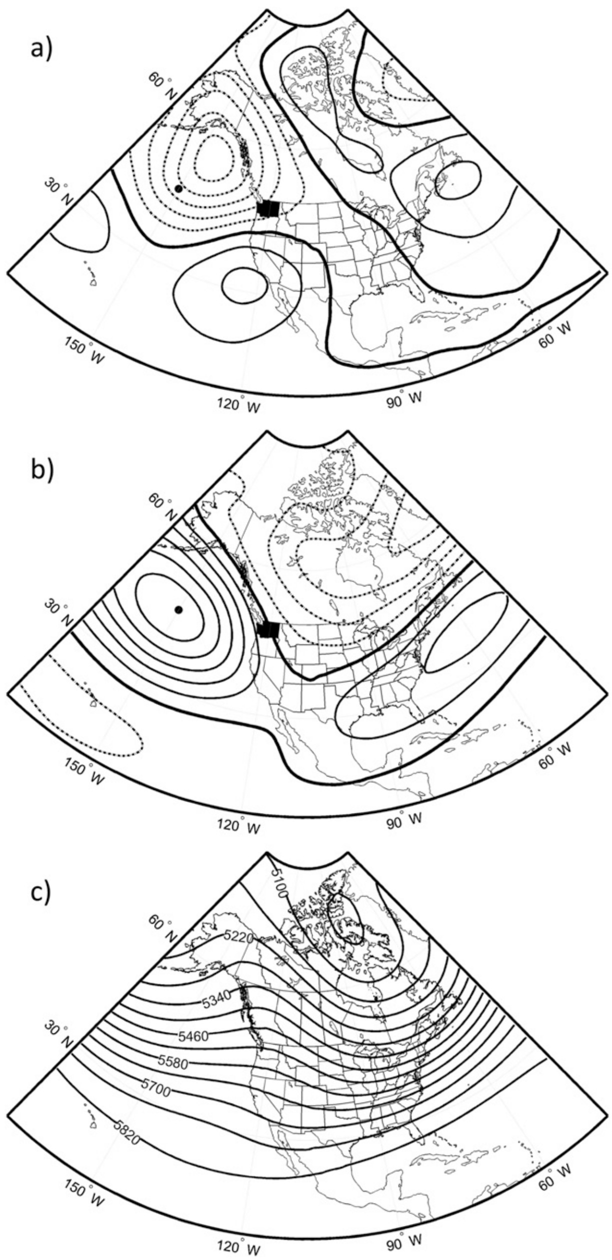


FIG. 2. (a) Covariance between DJF 500-hPa heights and the total precipitation index $T$, which is the sum of $P_1$ and $P_6$. Solid (dashed) contours represent positive (negative) covariance, spaced at 10 m. The bold contour represents zero covariance. A reference dot at 45°N, 150°W is shown to allow easier comparison with other figures. Washington State is shaded in black. (b) As in (a) but for the rain-shadow index $R$, which is the difference between $P_1$ and $P_6$. (c) The mean DJF 500-hPa height field from 1982 to 2010.

$P_6$, and then adding and subtracting those maps. Before discussing the maps in detail, it is important to note that they depict wintertime averages, and not the conditions that pertain during any one storm. In section 5 we present case studies of individual storms, which will illuminate the dynamical reasons for the statistical connections observed here.

The first covariance map (Fig. 2a) shows that a high value of $T$ (i.e., large overall precipitation in the Cascades) is associated with anomalously low geopotential heights over the Gulf of Alaska and a strengthening of the climatological ridge over southern California. In other words, more overall precipitation is associated with seasons of higher-than-average onshore flow (west-southwesterly over the Cascades), which is consistent with a higher flux of moisture into the region. Drier conditions are associated with the inverse of this pattern: weakened zonal flow, accompanied by high pressure in the Gulf of Alaska.

Figure 2a clearly shows that the large-scale circulation exerts a strong influence on $T$. To quantify the strength of this connection, we employ a statistical technique called "empirical orthogonal teleconnections 2" (EOT2), first described by van den Dool (2007). EOT2 is a method for calculating the maximum variance in a given time series (in this case, $T$) that can be explained by an independent variable (in this case, DJF 500-hPa heights) at a limited number of grid points. Using this technique, we find that 67% of the variance in $T$ is explained by 500-hPa heights at just two locations in the Gulf of Alaska and off the California coast, near the centers of maximum covariance in Fig. 2. This result is consistent with previous studies that found SLP to account for about 70% of the variability in Cascade snowpack (Stoelinga et al. 2010; Smoliak et al. 2010), providing further evidence that the large-scale circulation is the dominant control on Cascade wintertime precipitation.

A similarly strong connection with the atmospheric circulation is evident in the $R$ covariance map (Fig. 2b). There is a widespread response in 500-hPa heights over the northeastern Pacific, northeastern Canada, and the eastern seaboard of the United States. A strong rain shadow (high value of $R$) is associated with ridging well south of Alaska, meaning a more north-northwesterly component to the circulation. Conversely, a weak rain shadow is associated with the inverse of this pattern: a south-southeasterly wind anomaly that, on top of the mean pattern (Fig. 2c), results in weaker and more southerly flow into the Cascades. Applying the EOT2 technique to $R$ as we did to $T$, we find that 72% of the variance in $R$ is explained by 500-hPa heights—in this case at three grid points in the Pacific, Hudson Bay, and the Caribbean—proving that the strength of the wintertime rain shadow is also predominantly controlled by fluctuations in the large-scale circulation.

Since $T$ and $R$ are, by construction, orthogonal, we do not expect their associated circulation patterns to be

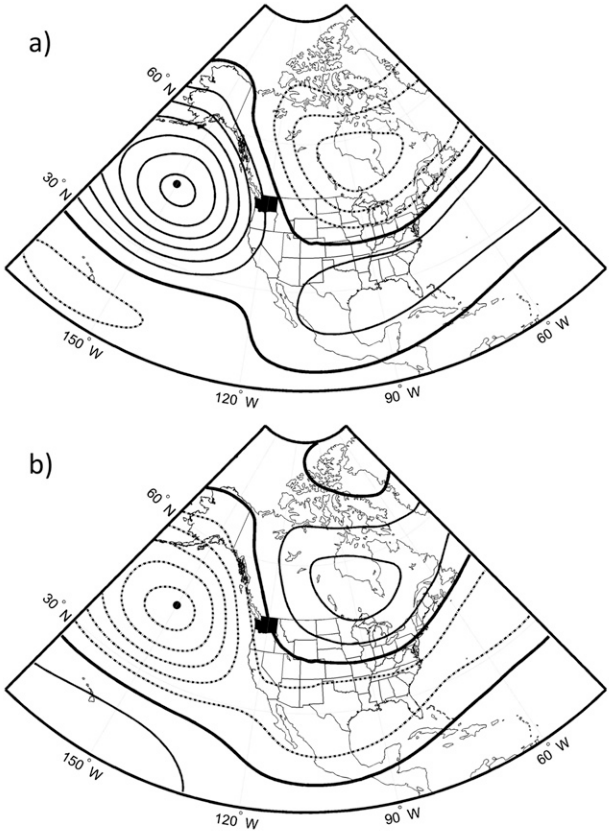


FIG. 3. (a) Covariance between DJF 500-hPa heights and the tropical–Northern Hemisphere (TNH) index. (b) Covariance between DJF 500-hPa heights and the Niño-3 index.

related to each other, and no striking connection is evident in Figs. 2a and 2b. Although the pattern in Fig. 2a does not appear to resemble any common mode of North Pacific variability that we are aware of, Fig. 2b is strikingly similar to the Tropical–Northern Hemisphere (TNH) pattern—a teleconnection pattern closely associated with ENSO (Mo and Livezey 1986; DeWeaver and Nigam 2002), shown in Fig. 3.

The connection between ENSO and the rain shadow is further supported by the correlations between $R$, the Niño-3 index, and the TNH index (Table 4). The correlations are both statistically significant and are at least 0.5 in magnitude. In contrast, $T$ is not significantly related to either ENSO or the TNH.

It should be noted that this result is consistent with previous research on Cascade precipitation. In particular, Leung et al. (2003) also found that correlations between ENSO and wintertime precipitation differ east and west of the Cascades, implying that ENSO must influence rain-shadow variability. However, our results do refute the widespread perception in the literature (e.g., Dettinger et al. 1998; Wright and Agee 2004; Ryu et al. 2009) and in the media that El Niño (La Niña) tends to bring drier (wetter) conditions to the entire Cascades. While this rule of thumb holds true from the crest westward, we find a negligible-to-opposite relationship between precipitation and ENSO on the eastern slopes.

TABLE 4. Correlation coefficients between the DJF average of $T$, $R$, the Niño-3 index, and the TNH index, from 1982 to 2010. Here $R$ is significantly correlated with the TNH and Niño-3 indices, while $T$ is not significantly correlated with either.

| | $T$ | $R$ | Niño-3 |
|---|---|---|---|
| Niño-3 | 0.03 | −0.50 | * |
| TNH | −0.20 | 0.63 | −0.66 |

At least two factors help explain why this misperception exists. Firstly, the western slopes have a higher density of weather stations than the eastern slopes, imparting a west-slope bias to any composite dataset of Cascade-average precipitation. Secondly, previous studies have mostly dealt with snowpack rather than precipitation per se. Because the southeasterly wind anomalies associated with El Niño (Fig. 3b) also tend to bring warmer temperatures, snowpack could decrease during El Niño despite higher precipitation on the eastern slopes, giving the false impression that El Niño brings drier conditions to all of the Cascades.

The connection between ENSO and the wintertime Cascade rain shadow may have implications for long-range forecasting. Because ENSO has strong persistence from autumn to winter, the November Niño-3 index is significantly predictive of wintertime rain-shadow strength, with a correlation coefficient of −0.56. In contrast, $T$, which is not related to a teleconnection pattern, has negligible persistence and is therefore impossible to forecast on monthly time scales. In other words, rain-shadow strength is more predictable than overall precipitation in the Cascades. As a result, the degree of predictability in wintertime precipitation is highly dependent on location relative to the crest. Predictability is highest for western slopes and far-eastern slopes where variability in $R$ accounts for a significant fraction of total variability. Predictability is much lower near the fulcrum of rain-shadow variability, where $T$ explains nearly all of the variance in wintertime precipitation (see Table 4). We discuss the implications of this for water resource management in the following section.

## 4. Watershed impacts

For water resources, the precipitation rates analyzed in the previous section are perhaps less important than streamflow. In contrast to the SNOTEL stations, which reflect only a single point in space, rivers integrate

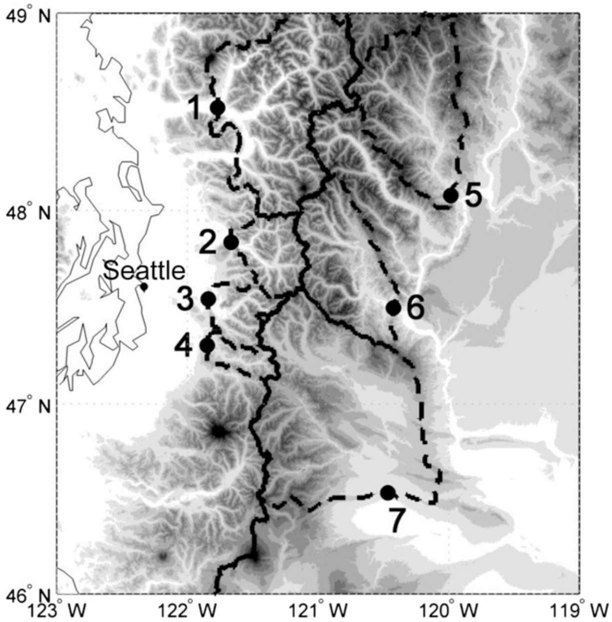


FIG. 4. A map of the watersheds considered in the analysis, with elevation represented by gray shading. Dashed lines mark the boundaries of the catchment areas upstream of the river gauges, denoted by black dots. The rivers are 1: Skagit, 2: Skykomish, 3: Snohomish, 4: Green, 5: Methow, 6: Wenatchee, and 7: Yakima. The USGS identification numbers of the river gauges are (1) 12194000, (2) 12134500, (3) 12144500, (4) 12106700, (5) 12449950, (6) 12462500, and (7) 12500450. The northern transect consists of rivers 1 and 5. The central transect consists of rivers 2 and 6. The southern transect consists of rivers 3, 4, and 7. The crest, which marks the boundary between western and eastern watersheds, is represented by a solid black line. Elevation is contoured in gray at intervals of 300 m as in Fig. 1.

precipitation over a broad catchment area and weight wetter locations more heavily than dry locations. Here we repeat the preceding analysis using data from streamflow gauges from the region's rivers. This has a twofold purpose. Firstly, it provides an additional check on the robustness of the results from the local SNOTEL measurements and, secondly, it allows us to evaluate the impact of rain-shadow variability on water resources.

We use data from U.S. Geological Survey (USGS) river gauges in the seven watersheds shown in Fig. 4. The dashed lines mark the extent of each gauge's catchment area, that is, the extent of the watershed lying upstream of the gauge. As an approximation of DJF precipitation in each basin, we use cumulative streamflow between December and the following August. In doing so, we obviously include precipitation falling outside DJF, thus diminishing the strength of any relationship with the DJF atmospheric circulation. However, a shorter interval would miss the substantial component of wintertime precipitation that falls as snow and is released from the landscape only during the melt season. To allow for direct comparison with the SNOTEL results, we limit our analysis to the same 28-yr period of the SNOTEL record.

The river gauges included in our analysis are not part of the Hydro-Climatic Data Network (HCDN), as the HCDN did not provide the spatial or temporal coverage necessary to allow direct comparison with the SNOTEL results. As a result, the data are susceptible to bias from possible changes in land use, river infrastructure, or irrigation practices. However, we are not aware of any such changes occurring upstream of our gauges over the 28-yr period of our study, nor are there any significant trends in the data to suggest otherwise. Moreover, while dams exist on the Skagit, Green, and Yakima Rivers, variability in the late-summer volume of the reservoirs behind these dams is a small fraction of each river's total annual streamflow. We are therefore confident that these river gauges provide an accurate representation of precipitation variability in the Cascades.

In place of $P_1$ and $P_6$ in the SNOTEL analysis, we use streamflow from western and eastern rivers. We divide the rivers into three transects according to latitude. The northern transect consists of the Skagit River on the west and the Methow River on the east. The central transect consists of the Skykomish River on the west and the Wenatchee River on the east. The southern transect consists of the Snohomish and Green Rivers on the west and the Yakima River on the east. For each of these transects, we calculate a total precipitation index ($T$) and a rain-shadow index ($R$) as before, normalizing the western and eastern time series and then taking their sum and difference.

The correlations between the western and eastern time series of the northern, central, and southern transects are 0.76, 0.86, and 0.78, respectively. These values are much higher than the correlation between $P_1$ and $P_6$ in the previous analysis (0.38), which is not surprising considering that much of the precipitation in eastern watersheds falls near the crest (Fig. 1), where it correlates strongly with western slopes (Table 1). Given these high correlations, $R$ is bound to account for a smaller fraction of the variance in streamflow than the 31% it contributes at SNOTEL sites 1 and 6 in section 3. Indeed, $R$ explains just 12%, 7%, and 11% of streamflow variance from north to south.

Despite its diminished contribution, however, the circulation patterns associated with $R$ are remarkably consistent among the three watershed transects (Fig. 5), and their structure is very similar to that of the analogous rain-shadow pattern from section 3 (Fig. 2b). The statistical significance of these patterns can be verified with EOT2 analysis, which shows that DJF 500-hPa

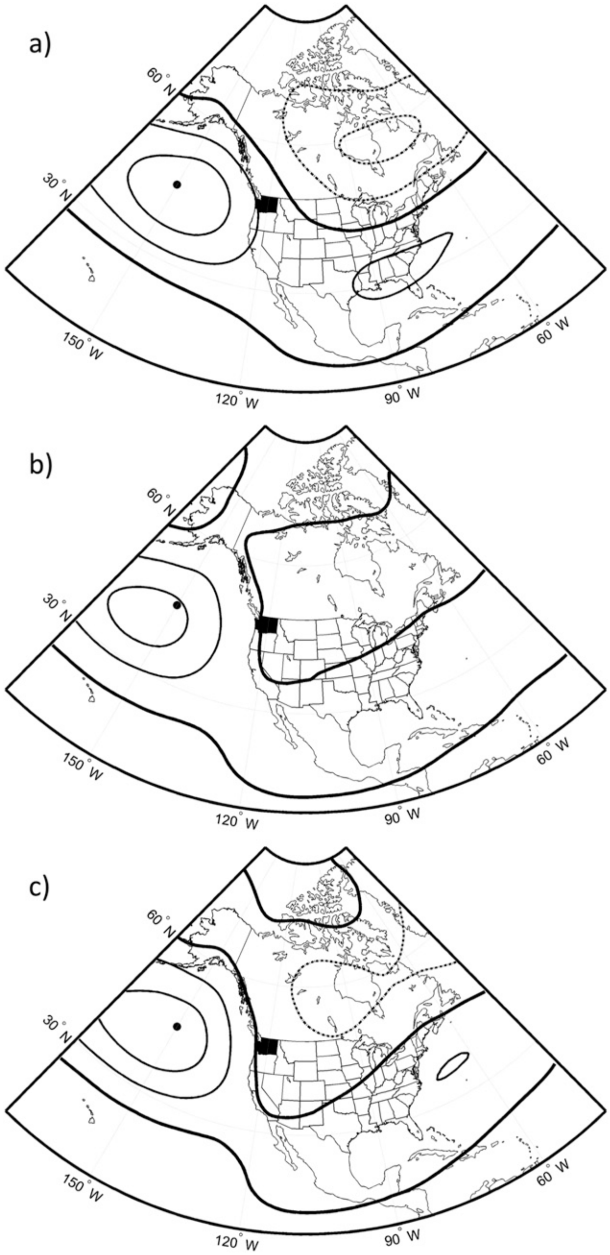


FIG. 5. As in Fig. 2b but substituting December–August streamflows in western and eastern watersheds for $P_1$ and $P_6$, respectively, for the (a) northern, (b) central, and (c) southern transects.

heights at just two grid points in the Gulf of Alaska and off the California coast explain at least 52% of the variability in $R$ at each transect, despite the additional noise that results from March–August precipitation being included in the streamflow data. Moreover, at each transect $R$ is significantly correlated with the DJF Niño-3 index, with correlation coefficients of $-0.54$, $-0.47$, and $-0.47$ from north to south. This confirms that a common circulation pattern, closely associated with the ENSO teleconnection, is primarily responsible for variability in rain-shadow strength across the Washington Cascades.

The circulation patterns associated with $T$ at each transect exhibit somewhat more variation while still maintaining much of the structure of Fig. 2a from the SNOTEL analysis. The $T$ circulation pattern of the northern transect (Fig. 6a) looks almost identical to Fig. 2a, with the same centers of action over the Gulf of Alaska, Nova Scotia, and the eastern Pacific near California. Similarly, the circulation patterns of the central and southern transects (Figs. 6b,c) also have three centers of action, though shifted somewhat from those in Fig. 2a.

Despite these broad similarities, however, one feature of the circulations in Figs. 6b and 6c stands out: their wind anomalies are northwesterly rather than southwesterly over the Cascades. There are two likely explanations for this difference. The first relates to topographic differences upstream of the western watersheds. Because of the rain-shadowing effects of Mt. Rainier and the Olympic Mountains, southwestern watersheds like the Green (number 4 in Fig. 4) tend to receive maximum precipitation during zonal flow, while northwestern watersheds like the Skagit (1) tend to receive maximum precipitation during west-southwesterly flow (Neiman et al. 2011). While this difference is modest, it likely contributes to the differences in $T$ patterns observed in Fig. 6.

The second reason for the differences in $T$ patterns among the three transects relates to the geometries of the eastern watersheds. While the Wenatchee (6) and Yakima (7) basins share long borders with the crest, the Methow (5) lies mostly east of the crest. Consequently, the Wenatchee and Yakima draw more of their water from near the crest where precipitation is more strongly correlated with western slopes. As a result, their $T$ patterns are weighted more heavily toward a western precipitation signal, contributing to the observed northwesterly flow anomalies in Figs. 6b and 6c.

The watershed data are fully consistent with the results presented from the single SNOTEL transect in section 3. The rain-shadow pattern is very robust, with little variation from one transect to another. The pattern associated with total precipitation exhibits some variability among the transects, but these differences are easily understood in light of the different watershed geometries. Such consistency suggests that the SNOTEL transect analyzed in section 3 is, in fact, representative of the Washington Cascades more generally, and that wintertime precipitation in the Cascades is well characterized by just two modes of variability: a total precipitation mode $T$ and a rain-shadow mode $R$.

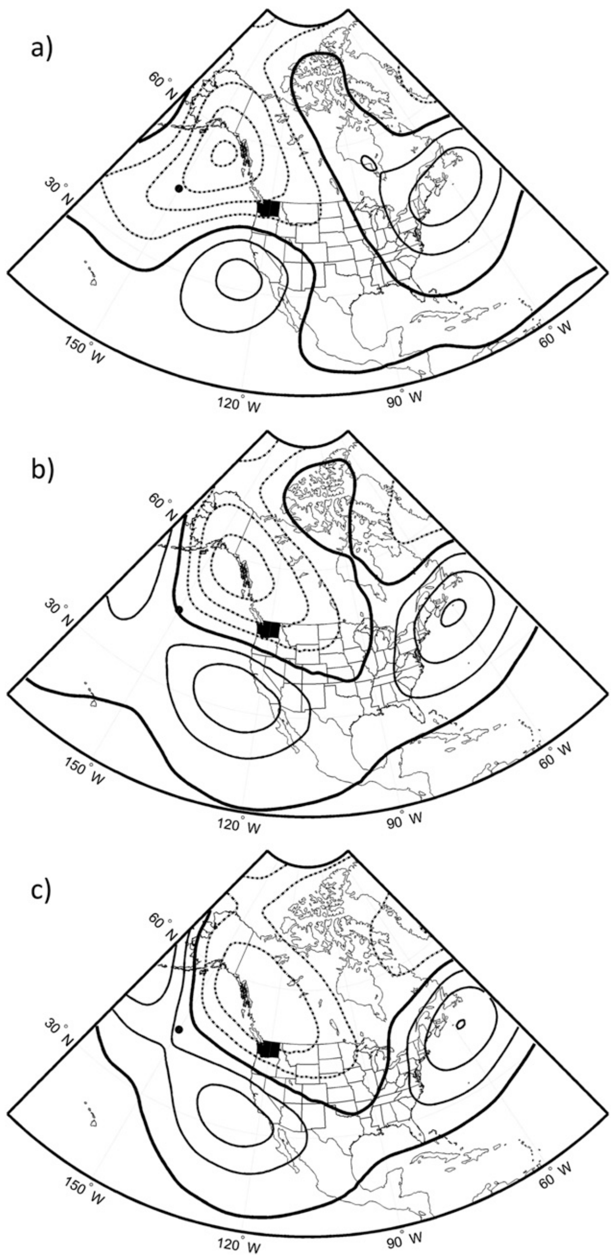


FIG. 6. As in Fig. 2a but substituting December–August streamflows in western and eastern watersheds for $P_1$ and $P_6$, respectively, for the (a) northern, (b) central, and (c) southern transects.

A full assessment of the impact of rain-shadow variability on water resources would require a further and extensive analysis of temperature, snowpack, and other variables that influence the hydrological cycle. Nevertheless, two aspects of the preceding analysis are relevant to water resources and should be emphasized. Firstly, differences in streamflow variability east and west of the crest, while relatively small, are caused primarily by circulation patterns associated with ENSO variability. Secondly, we showed in the previous section that rain-shadow variability (and thus ENSO) is least important just east of the crest near the fulcrum of the rain-shadow mode. This implies a weak connection between ENSO and eastern streamflows, as confirmed by the low correlations between the Niño-3 index and annual streamflows in the Methow, Wenatchee, and Yakima Rivers ($|r| \leq 0.18$). As a result, annual streamflows east of the crest are inherently less predictable than annual streamflows west of the crest, where ENSO influence on precipitation is unambiguous.

## 5. Dynamics

In the preceding analysis, we demonstrated that ENSO via its TNH-like teleconnection pattern plays an important role in controlling the strength of the wintertime Cascade rain shadow. We now examine this connection more closely, focusing on how variability in the large-scale circulation translates into variability in the dynamics of individual storms.

Our dataset consists of six years of archived forecast output between 2005 and 2010. Two different weather prediction models were used: the fifth-generation Pennsylvania State University–National Center for Atmospheric Research Mesoscale Model (MM5) and the Weather Research and Forecasting model (WRF). The MM5 model was run twice daily by the Northwest Regional Modeling Consortium at the University of Washington from 1997 until it was replaced by the WRF model on 15 April 2008. Both models were run at 4-km horizontal resolution and initialized with output from the National Centers for Environmental Prediction Global Forecast System (GFS) model. Several changes were made to the models between 2005 and 2010, most notably to the microphysics parameterization scheme in May 2006. All model changes are documented at http://www.atmos.washington.edu/mm5rt/log.html.

Within the six years of model output, we have chosen to focus exclusively on the 100 strongest storms, defined as the 100 24-h periods during when the most precipitation fell in the Washington Cascades (defined, for our purposes, as the region within the box in Fig. 7a). These storms were identified as follows. First, using gridded precipitation output at 6-h intervals (corresponding to 0000, 0600, 1200, and 1800 UTC), we calculated the 24-h running mean of cumulative precipitation in the Washington Cascades. Storms were then identified as the 100 largest relative maxima in the running-mean time series. If multiple relative maxima occurred within a 48-h period, only the largest was included in our dataset. Together, these 100 storms account for 32% of the total

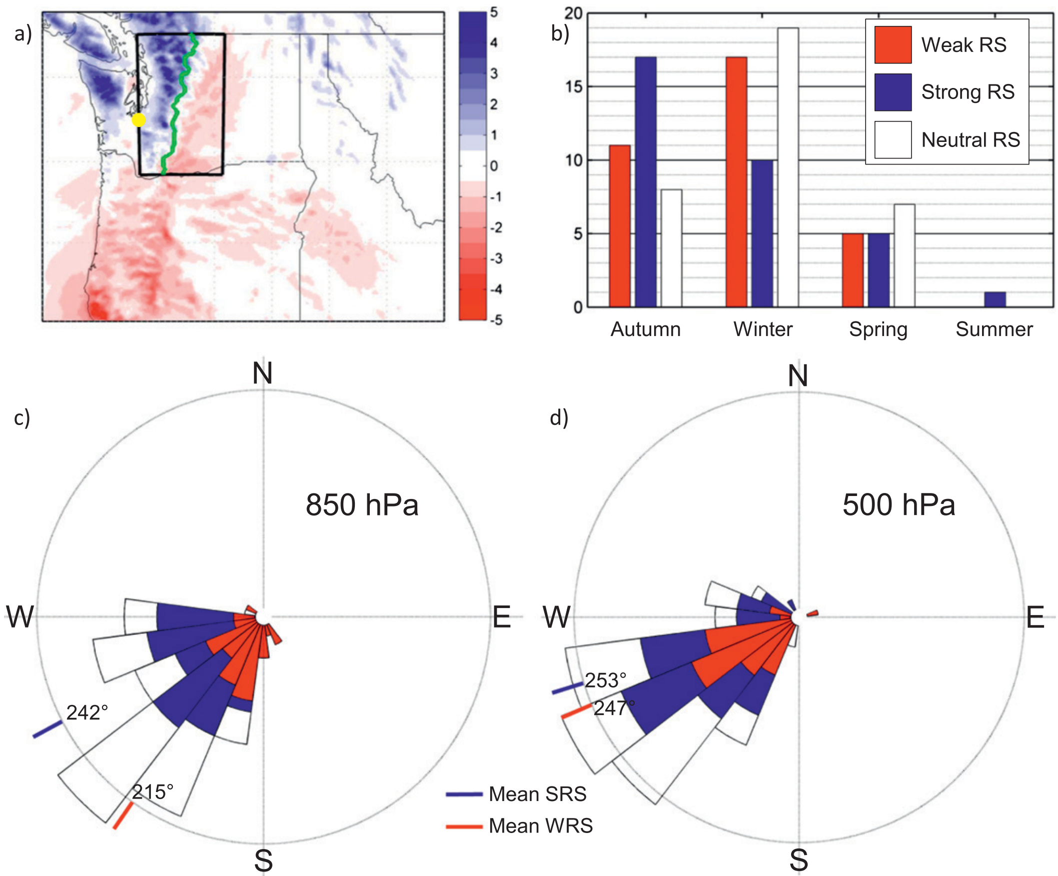


FIG. 7. (a) The difference in average precipitation (cm) between the 33 strongest-rain-shadow storms and the 33 weakest-rain-shadow storms out of the 100 wettest storms in the Washington Cascades from 2005 to 2010. Positive (negative) values indicate more precipitation during strong-rain-shadow (weak-rain-shadow) storms. The black box represents the region within the model over which precipitation was summed to calculate total storm precipitation. The green line represents the crest of the Washington Cascades. (b) The number of storms with weak (red), strong (blue), and neutral (white) rain shadows by season. Weak-rain-shadow (strong-rain-shadow) storms are the 33 storms with the lowest (highest) rain-shadow index values among the 100 wettest storms from 2005 to 2010. The seasons are defined as follows: autumn (SON), winter (DJF), spring (MAM), and summer (JJA). (c) The distribution of 850-hPa wind direction during storms with weak (red), strong (blue), and neutral (white) rain shadows. The distribution represents the model output at the grid point marked by the yellow dot in (a), at the beginning of the wettest 12-h period of each storm. The radius of each pie wedge is proportional to the number of storms with winds coming from the direction of the wedge. The lines abutting the edge of the circle indicate the mean wind direction of SRS storms (blue) and WRS storms (red). (d) As in (c) but for 500-hPa winds.

precipitation in the Cascade region between 2005 and 2010.

As a measure of rain-shadow strength for each storm, we have calculated a rain-shadow index $R$—just as we did previously—by normalizing the time series of western and eastern precipitation over the 100-storm dataset and taking their difference (see Fig. 7a for the western and eastern domains). By this metric high values of $R$ indicate strong rain shadows, while low values of $R$ indicate weak rain shadows. To facilitate comparison between storms with strong and weak rain shadows, we divided our dataset into three categories. The 33 storms with the highest $R$ values were defined as strong-rain-shadow (SRS) storms, while the 33 storms with the lowest $R$ values were defined as weak-rain-shadow (WRS) storms. The remaining 34 storms in our dataset are considered neutral-rain-shadow (NRS) storms.

### a. *Influence of storm-track latitude*

How does ENSO influence rain-shadow strength in the Washington Cascades? It is well established that the overall storm track is shifted southward in El Niño winters relative to La Niña winters (e.g., Horel and Wallace 1981; van Loon and Rogers 1981; Seager et al.

2010; Lareau and Horel 2012). Several lines of evidence, presented in Fig. 7, suggest that it is indeed this shift that explains the changes in rain-shadow strength.

Firstly, Fig. 7a shows the difference in average precipitation between SRS and WRS storms over the entire model domain. As expected, a see-saw pattern is evident in the Washington Cascades, meaning that SRS storms bring more precipitation to western slopes, and less precipitation to eastern slopes, than WRS storms. However, significant differences are also observed in southwestern Oregon, which receives nearly 5 cm more precipitation during WRS storms than during SRS storms. In other words, storms that exhibit weak rain shadows in the Washington Cascades also tend to bring more precipitation south of Washington. This implies a more southern path for the intense precipitation.

Secondly, seasonal variations are also supportive of the same connection (Fig. 7b). In autumn nearly half (47%) of all storms are SRS storms, while 31% are WRS storms. In winter, on the other hand, WRS storms are more common, accounting for 37% of the total compared to just 22% that are SRS storms. The preponderance of SRS storms in autumn and WRS storms in winter is consistent with the southward migration of the Pacific storm track from autumn to winter (Chang et al. 2002; Lareau and Horel 2012).

Finally, differences in storm-track latitude are also implicated by the differences in wind direction between storm types (Figs. 7c,d). WRS storms on average exhibit more southerly winds at 850 hPa and stronger veering between 850 and 500 hPa. The veering in particular suggests that warm-air advection may be stronger during WRS storms than during SRS storms. Using the equation for thermal wind [e.g., Holton 2004, Eq. (3.31)], we confirm that WRS storms on average exhibit twice as much warm-air advection as SRS storms ($\mathbf{u} \cdot \nabla T = 0.62$ versus 0.31 K h$^{-1}$). This suggests that WRS storms are more common during warm-frontal passage while SRS storms are more common when temperature advection is weaker, as is typical in a storm's warm sector. Because warm fronts lie to the north of the warm sector in a midlatitude cyclone, warm-sector precipitation in the Washington Cascades should be more likely with a northern storm track, while warm-frontal precipitation should be more likely with a southern storm track.

To confirm the connection between the type of precipitation (i.e., warm frontal versus warm sector) and rain-shadow strength, we examined the synoptic features of the 10 strongest SRS storms and the 10 weakest WRS storms, using a combination of ECMWF reanalysis data and surface analyses from the National Weather Service (NWS). As expected, we found that precipitation in the Washington Cascades occurred primarily in the warm sector of all 10 SRS storms, while not a single WRS storm involved significant warm-sector precipitation. Of the 10 WRS storms, 7 brought the heaviest precipitation ahead of either a warm or partially occluded front accompanied by significant warm-air advection. The remaining three followed the southernmost paths of all, making landfall near the mouth of the Columbia River and generating southeasterly winds in the Washington Cascades, effectively reversing the climatological rain shadow.

How might warm fronts act to weaken the rain-shadow effect? An analysis of the mesoscale structure of WRS storms suggests that they often exhibit weak and/or shallow mountain waves, with correspondingly weak vertical velocities that dampen both windward condensation and leeward evaporation. There are at least three ways that warm fronts can have this effect. Firstly, veering during warm-frontal passage can create a directional critical level, causing mountain wave amplitude to decay with height (e.g., Shutts 1995, 1998; Doyle and Jiang 2006). Secondly, a warm front is often associated with high static stability at low levels, which can lead to orographic blocking and lower-amplitude mountain waves (Smith et al. 2002). Finally, a decline in static stability with height, which typically occurs above a warm-frontal zone, reduces the index of refraction for mountain waves (also known as the ''Scorer parameter''), which in turn can cause the waves to be trapped, limiting their vertical extent (Scorer 1949; Sawyer 1960). In the following case studies, we present empirical evidence that these three mechanisms do, in fact, contribute to weakening the Cascade rain shadow during warm-frontal passages.

### b. Case studies

Here we focus on two storms that clearly illustrate the mechanisms by which warm-sector (warm frontal) precipitation favors a strong (weak) rain shadow. The first storm, which had the seventh-strongest rain shadow of all storms in the dataset, took place 3–4 December 2007, with maximum precipitation in the Washington Cascades occurring from 1200 to 1800 UTC on 3 December. The second storm, which had the fourth-weakest rain shadow of all storms in the dataset, took place 31 January–1 February 2006, with maximum precipitation in the Washington Cascades occurring from 0300 to 0900 UTC on 1 February. We chose to compare these storms because they have the same wind direction near crest level along a southwest-to-northeast transect through the central Cascades and, therefore, provide the cleanest possible comparison between warm-frontal and warm-sector precipitation. We restrict our analysis to the 6-h period of maximum precipitation in each storm.

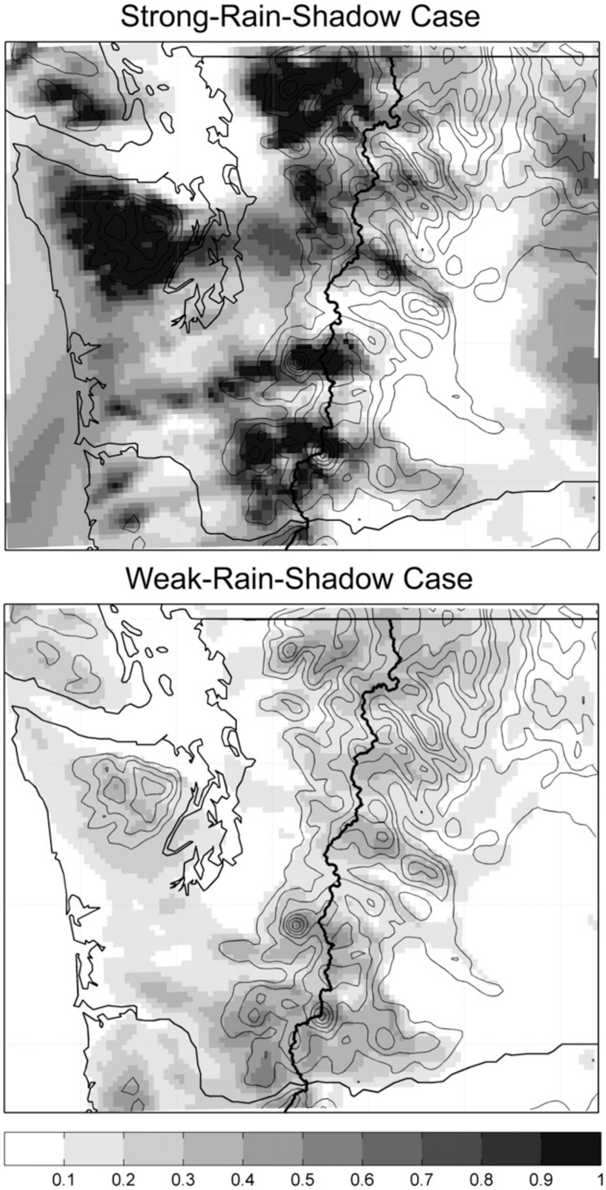


FIG. 8. Average hourly precipitation in cm during the 6 h of maximum precipitation for (top) the strong-rain-shadow and (bottom) the weak-rain-shadow case. The periods are SRS case: 1200–1800 UTC on 3 Dec 2007 and WRS case: 0300–0900 UTC on 1 Feb 2006. A black line marks the crest. Source is the MM5 model, 4-km resolution.

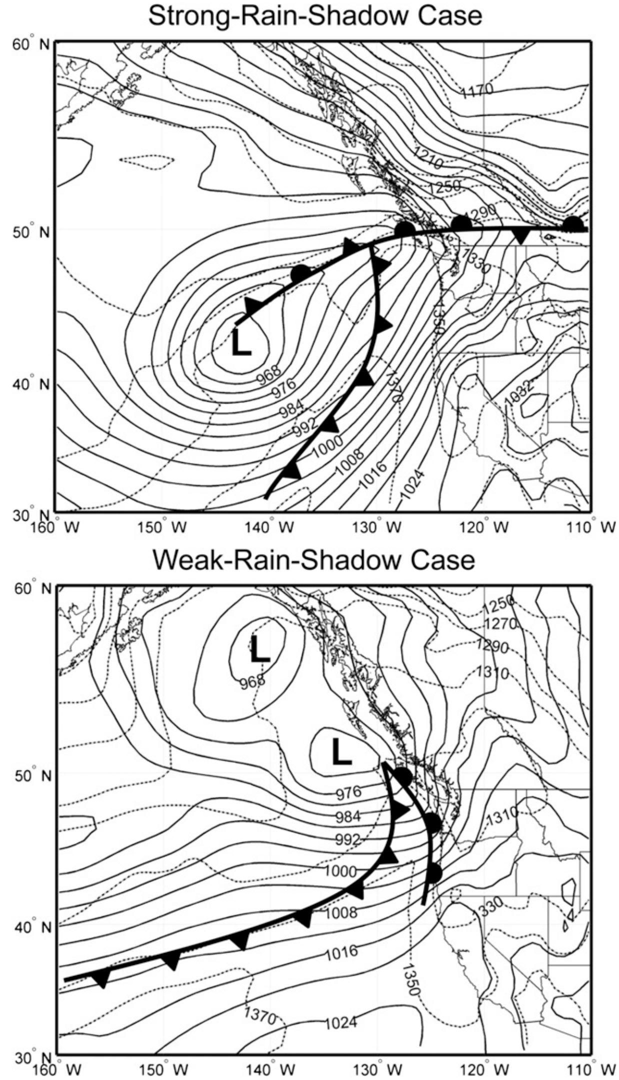


FIG. 9. Sea level pressure (solid contours, hPa) and 1000–850-hPa thickness (dotted contours, m) at the beginning of the 6-h period of maximum precipitation for (top) the SRS and (bottom) the WRS case. Strong gradients in the thickness field indicate the presence of fronts. In the SRS case, the Cascades lie within the warm sector where little warm-air advection occurs, while significant warm-air advection accompanies the warm front in the WRS case. Source is the ERA-Interim dataset.

Average precipitation rates during each 6-h window are shown in Fig. 8. Note that the widespread pattern of precipitation in the WSR case cannot be produced by a simple enhancement in precipitation spilling over the crest of the Cascades.

Figure 9 shows SLP and 1000–850-hPa thickness at the beginning of each storm's 6-h window. The thickness field is proportional to lower tropospheric temperature, so strong gradients delimit fronts, which we have drawn with additional guidance from NWS surface analyses. Consistent with the inferences made previously, the Cascades lay within the warm sector of the SRS case, while precipitation in the WRS case occurred when there was an approaching warm front.

To assess the extent to which synoptic-scale ascent contributes to the differences in rain-shadow strength between the two storms, we compare each storm's 500-hPa vertical velocity in Fig. 10. Data plotted are for hour 3 of

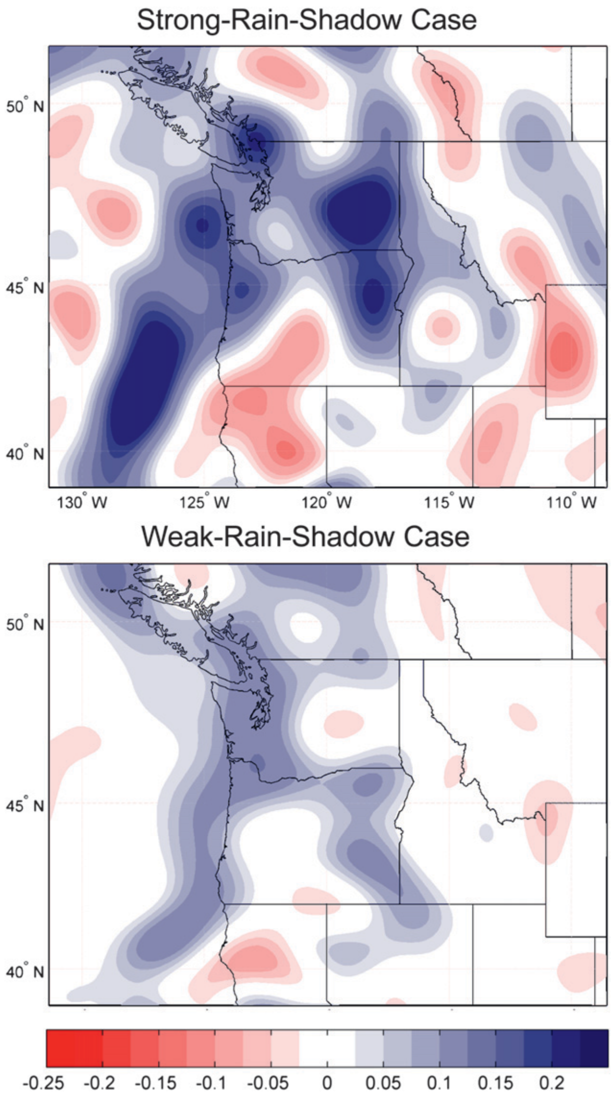


FIG. 10. Synoptic-scale 500-hPa vertical velocity (m $s^{-1}$) at hour 3 of the 6-h period of maximum precipitation for (top) the SRS and (bottom) the WRS case. The data were filtered to remove wavelengths less than 240 km.

each storm's 6-h window, and all wavelengths less than 240 km have been filtered out. The SRS case clearly exhibits stronger ascent overall,consistent with its larger precipitation totals (Fig. 8). However, the patterns of ascent are precisely the opposite of what one might expect from the precipitation distributions in Fig. 8: in the SRS case, ascent is more or less evenly distributed across the Cascades, while in the WRS case, ascent is concentrated over Puget Sound and the western slopes of the Cascades. These patterns of synoptic-scale ascent cannot account for the observed differences in rain-shadow strength, suggesting that differences are generated by smaller-scale dynamical processes.

Figures 11 and 12 show various mesoscale details of the two storms at hour 1 (top), 3 (middle), and 5 (bottom) of each storm's 6-h window of maximum precipitation. In the left column, barbs represent the average winds at 900 hPa (black), 800 hPa (red), and 500 hPa (blue), while green/yellow shading indicates where the 700-hPa vertical wind exceeds 0.5 m $s^{-1}$ in magnitude. The center column shows a vertical cross section of liquid and ice water content (LIWC) and vertical winds along the 200-km transect between points A and B in the left column. The black dot represents the center of the transect, where at 775 hPa the winds of both storms are oriented parallel to the transect. Finally, the right column represents the vertical profile of static stability just upwind of the transect, calculated using the Durran and Klemp (1982) approximation for the moist Brunt–Väisälä frequency $N$.

Beginning with the SRS case (Fig. 11), little change is observed between hour 1 and 5, which is not surprising given the absence of significant temperature advection. Weak vertical gradients in wind and static stability allow vigorous mountain waves to penetrate the entire tropospheric column. In the vertical cross section (center column), there is a clear relationship between the mountain wave pattern and LIWC, with upward (downward) vertical motion corresponding to an increase (decrease) in LIWC along the transect. A particularly sharp decrease in LIWC is evident at the Cascade crest near the center of the transect where downward vertical velocities as high as 3 m $s^{-1}$ are observed. This results in a sharp precipitation gradient between windward and leeward slopes and, thus, a strong rain shadow.

In contrast to the SRS case, the WRS case is a good example of how a warm-frontal passage can weaken the rain-shadow effect (Fig. 12). Early in the storm strong veering between 800 and 500 hPa imposes a directional critical level near 500 hPa, capping the extent of mountain wave penetration. High static stability ($N$ ~0.015 $s^{-1}$) below 800 hPa suggests that the flow may also be blocked, resulting in low-level southerly flow west of the Cascades that further dampens mountain wave activity. At hours 1 and 3 static stability dramatically decreases above the frontal zone (~850 hPa), resulting in a sharp reduction in the Scorer parameter that likely helps to confine the waves near the surface. At hour 5, after the front has passed and veering is diminished, wave dampening persists because of vertical wind shear, which maintains a strong vertical gradient in the Scorer parameter. With weak vertical winds the WRS case exhibits only a modest decline in LIWC downstream of the crest, resulting in a relatively uniform distribution of precipitation between leeward and windward slopes, despite weak synoptic-scale ascent in the lee (Fig. 10).

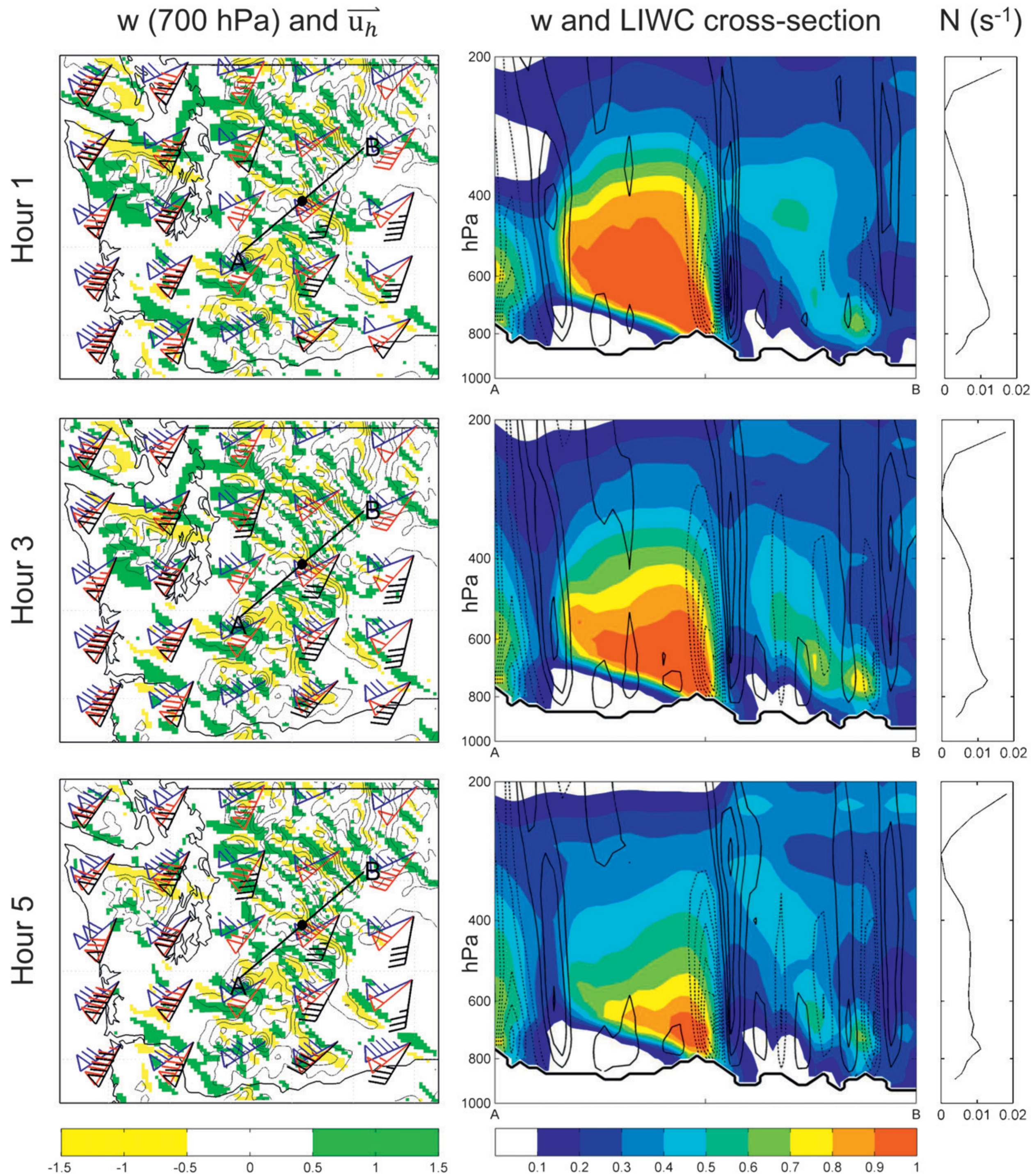


FIG. 11. Wind, moisture, and static stability at hour (top) 1, (middle) 3, and (bottom) 5 of the SRS case. (left) Wind barbs show horizontal winds at 900 hPa (black), 800 hPa (red), and 500 hPa (blue). Green (yellow) shading indicates where upward (downward) vertical winds exceed 0.5 m s$^{-1}$ at 700 hPa. A 200-km transect is shown in black between points A and B, with a dot marking the center point. At 775 hPa, over the center point the average wind direction of both storms is parallel to the transect. (center) Vertical cross sections of liquid/ice water and vertical winds along the 200-km transect between points A and B in the left. Colored contours depict the liquid plus ice mixing ratio (g kg$^{-1}$). Solid (dashed) contours represent upward (downward) vertical winds at intervals of 0.5 m s$^{-1}$. (right) Moist Brunt–Väisälä frequency averaged over a 9000 km$^2$ area just upstream of the transect. Source is the MM5 model, 4-km resolution.

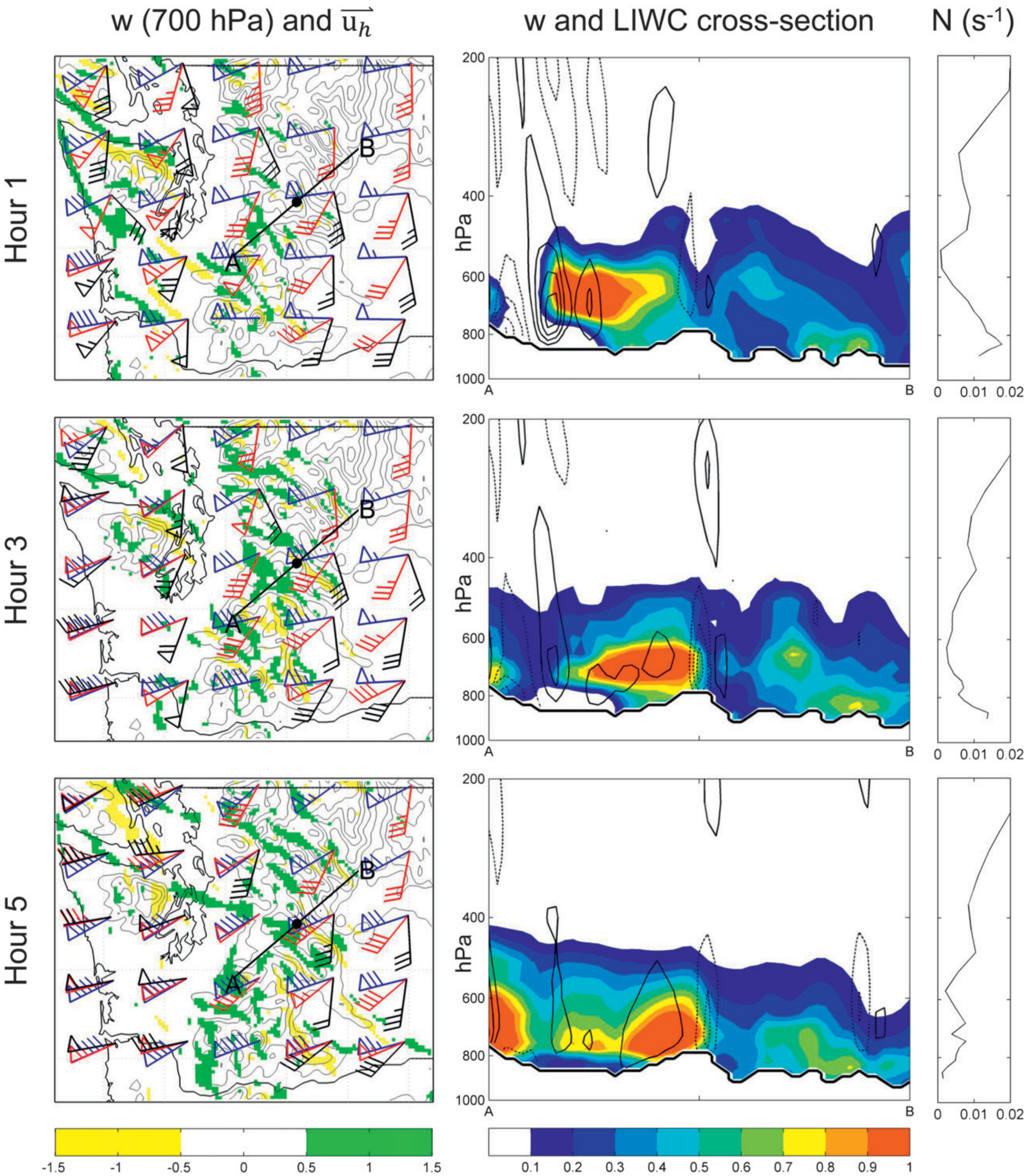


FIG. 12. As in Fig. 11 but for the WRS case.

From these two cases, it seems clear that much of the variability in Cascade rain-shadow strength can be attributed to differences in mountain wave activity between warm-sector and warm-frontal storms. In warm-sector storms weak temperature advection presents ideal conditions for deep mountain waves to form, resulting in large precipitation gradients between windward and leeward slopes. In warm-frontal storms warm-air advection causes strong vertical gradients in both wind and static stability, leading to weaker mountain waves and a more uniform precipitation distribution.

## 6. Discussion

In this paper, we have shown that interannual variability in wintertime Cascade precipitation can be characterized by two orthogonal indices: a total precipitation index ($T$) representing regionwide precipitation and a rain-shadow index ($R$) representing the strength of the east–west precipitation gradient. While $T$ explains the majority of the variance in interannual wintertime precipitation, $R$ explains up to 31% of the variance on western and far-eastern slopes.

Variability in the large-scale circulation explains about 70% of the variability in both $T$ and $R$. The circulation pattern associated with $T$ has no known forcing: it appears to result from stochastic weather processes that have negligible persistence on seasonal time scales. In contrast, $R$ is strongly influenced by a teleconnection pattern associated with ENSO and, therefore, exhibits significant predictability from autumn to winter. For streamflows this means that predictability is only significant for western watersheds where the influence of $R$ (and thus ENSO) is unambiguous.

Several lines of evidence suggest that ENSO influences rain-shadow strength by controlling the latitude of the Pacific storm track. A northern storm track associated with La Niña brings more warm-sector precipitation to the Washington Cascades, creating ideal conditions for deep mountain waves that enhance the rain-shadow effect. During El Niño a southern storm track brings more warm fronts through the Cascades, which are often accompanied by weak mountain waves and a weak rain shadow. Three mechanisms likely contribute to suppressing mountain wave activity during warm-frontal passage: enhanced veering due to warm-air advection, enhanced blocking due to low-level stability, and a sharp decline in the Scorer parameter above the frontal zone, where static stability is significantly reduced. While all of these mechanisms appear to have been at work in the weak-rain-shadow storm of 31 January 2006, as well as the others that we examined, the relative importance of each mechanism to rain-shadow variability in the Cascades—or elsewhere—has yet to be determined conclusively.

Our results demonstrate the importance of understanding the detailed synoptic and mesoscale dynamics involved in rain-shadow variability. Time-averaged fields provide little indication of the synoptic conditions under which precipitation occurs. There is a danger that interpretations based on the wintertime-mean circulation may not give the full picture (e.g., Leung et al. 2003).

How generally might the results of this study apply to other midlatitude ranges with strong rain shadows? The connection between ENSO and rain-shadow strength is probably specific to the Cascades where fluctuations in storm-track latitude can have a significant impact on the ratio of warm-sector to warm-frontal precipitation. The Cascades are also lower in elevation than other rain-shadowed ranges such as the Andes, the Southern Alps, and the Sierra Nevada, which may further limit the generality of our results. Indeed, in both the Southern Alps and Sierra Nevada, heavy leeside precipitation has been linked, not to warm-frontal passages, but to strong cross-barrier flow advecting moisture to the lee (Sinclair et al. 1997; Underwood et al. 2009). Nevertheless, there is reason to believe that at least some of the mechanisms identified in this study may influence rain-shadow strength elsewhere. Blocking, static stability, and vertical wind shear have all been shown to modify precipitation patterns on the windward slopes of various mountain ranges (e.g., Colle 2004; Dettinger et al. 2004; Rotunno and Houze 2007), and it would not be surprising to find that their influence extends to the lee side as well. In the absence of detailed studies of other mountain ranges, however, there is currently insufficient evidence to conclude that the controls on rain-shadow variability in the Cascades must also apply to other mountain ranges.

Our results may have important implications for the impacts of climate change on Cascade precipitation. Several models predict an El Niño–like change in the mean-state circulation of the North Pacific due to a weakening of the Walker circulation and a reduction in the east–west gradient in tropical Pacific sea surface temperatures (e.g., Meehl et al. 2006; Stevenson et al. 2012). If these models are correct, we might expect the eastern slopes of the Cascades to receive more wintertime precipitation in response to climate change and the western slopes to receive less precipitation. Indeed, Salathé et al. (2010) found precisely this result in regional simulations forced by two different global climate models. However, significant variance remains among model projections of the mean-state circulation and the ENSO teleconnection in a warmer world (Collins et al. 2010). Unless models improve, all we can say with confidence is that any change in the large-scale circulation may well have a very different impact on precipitation east and west of the Cascade crest. At a more general level, understanding controls on the strength of the rain shadow is representative of a broader challenge in climate science: in regions of extreme gradients small changes in the overall circulation can give rise to a large local response. If the impacts of climate change in such regions are to be forecasted accurately, a combination of improved dynamical understanding and narrower constraints from model projections is required.

*Acknowledgments.* Neal Johnson provided invaluable support gathering archived MM5 and WRF data from the Northwest Regional Modeling Consortium. Justin Minder, Ron Smith, Mike Wallace, and two anonymous reviewers provided helpful comments that improved the manuscript. This work was supported by the National Defense Science and Engineering Graduate Fellowship. DRD's contribution was supported by National Science Foundation Grants ATM-0836316 and AGS-1138977.

## REFERENCES

Casola, J. H., L. Cuo, B. Livneh, D. P. Lettenmaier, M. T. Stoelinga, P. W. Mote, and J. M. Wallace, 2009: Assessing the impacts of global warming on snowpack in the Washington Cascades. *J. Climate,* **22,** 2758–2772.

Chang, E. K. M., S. Lee, and K. L. Swanson, 2002: Storm-track dynamics. *J. Climate,* **15,** 2163–2183.

Chater, A. M., and A. P. Sturman, 1998: Atmospheric conditions influencing the spillover of rainfall to lee of the Southern Alps, New Zealand. *Int. J. Climatol.,* **18,** 77–92.

Colle, B. A., 2004: Sensitivity of orographic precipitation to changing ambient conditions and terrain geometries: An idealized modeling perspective. *J. Atmos. Sci.,* **61,** 588–606.

Collins, M., and Coauthors, 2010: The impact of global warming on the tropical Pacific Ocean and El Niño. *Nat. Geosci.,* **3,** 391–397.

Dee, D. P., and Coauthors, 2011: The ERA-Interim reanalysis: Configuration and performance of the data assimilation system. *Quart. J. Roy. Meteor. Soc.,* **137,** 553–597.

Dettinger, M. D., D. R. Cayan, H. F. Diaz, and D. M. Meko, 1998: North–south precipitation patterns in western North America on interannual-to-decadal timescales. *J. Climate,* **11,** 3095–3111.

——, K. Redmond, and D. Cayan, 2004: Winter orographic precipitation ratios in the Sierra Nevada: Large-scale atmospheric circulations and hydrologic consequences. *J. Hydrometeor.,* **5,** 1102–1116.

DeWeaver, E., and S. Nigam, 2002: Linearity in ENSO's atmospheric response. *J. Climate,* **15,** 2446–2461.

Doyle, J. D., and Q. Jiang, 2006: Observations and numerical simulations of mountain waves in the presence of directional wind shear. *Quart. J. Roy. Meteor. Soc.,* **132,** 1877–1905.

Durran, D. R., and J. B. Klemp, 1982: On the effects of moisture on the Brunt–Väisälä frequency. *J. Atmos. Sci.,* **39,** 2152–2158.

Hayes, P. S., L. A. Rasmussun, and H. Conway, 2002: Estimating precipitation in the central Cascades of Washington. *J. Hydrometeor.,* **3,** 335–346.

Holton, J. R., 2004: *An Introduction to Dynamic Meteorology.* 4th ed. Academic Press, 535 pp.

Horel, J. D., and J. M. Wallace, 1981: Planetary-scale atmospheric phenomena associated with the Southern Oscillation. *Mon. Wea. Rev.,* **109,** 813–829.

Kaplan, M. L., C. S. Adaniya, P. J. Marzette, K. C. King, S. J. Underwood, and J. M. Lewis, 2009: The role of upstream midtropospheric circulations in the Sierra Nevada enabling leeside (spillover) precipitation. Part II: A secondary atmospheric river accompanying a midlevel jet. *J. Hydrometeor.,* **10,** 1327–1354.

Lareau, N. P., and J. D. Horel, 2012: The climatology of synoptic-scale ascent over western North America: A perspective on storm tracks. *Mon. Wea. Rev.,* **140,** 1761–1778.

Leung, L. R., Y. Qian, X. Bian, and A. Hunt, 2003: Hydroclimate of the western United States based on observations and regional climate simulation of 1981–2000. Part II: Mesoscale ENSO anomalies. *J. Climate,* **16,** 1912–1928.

Meehl, G. A., H. Teng, and G. Branstator, 2006: Future changes of El Niño in two global coupled climate models. *Climate Dyn.,* **26,** 549–566.

Mo, K. C., and R. E. Livezey, 1986: Tropical–extratropical geopotential height teleconnections during the Northern Hemisphere winter. *Mon. Wea. Rev.,* **114,** 2488–2515.

Mote, P. W., and Coauthors, 1999: Impacts of climate variability and change in the Pacific Northwest. JISAO Climate Impacts Group Tech. Rep., 109 pp.

Neiman, P. J., L. J. Schick, F. M. Ralph, M. Hughes, and G. A. Wick, 2011: Flooding in western Washington: The connection to atmospheric rivers. *J. Hydrometeor.,* **12,** 1337–1358.

Robertson, A. W., and M. Ghil, 1999: Large-scale weather regimes and local climate over the western United States. *J. Climate,* **12,** 1796–1813.

Roe, G. H., 2005: Orographic precipitation. *Annu. Rev. Earth Planet. Sci.,* **33,** 645–671.

Rotunno, R., and R. A. Houze, 2007: Lessons on orographic precipitation from the Mesoscale Alpine Programme. *Quart. J. Roy. Meteor. Soc.,* **133,** 811–830.

Ryu, J. H., M. D. Svoboda, J. D. Lenters, T. Tadesse, and C. L. Knutson, 2009: Potential extents for ENSO-driven hydrologic drought forecasts in the United States. *Climatic Change,* **101,** 575–597.

Salathé, E. P., L. R. Leung, Y. Qian, and Y. Zhang, 2010: Regional climate model projections for the state of Washington. *Climatic Change,* **102,** 51–75.

Sawyer, J. S., 1960: Numerical calculation of the displacements of a stratified airstream crossing a ridge of small height. *Quart. J. Roy. Meteor. Soc.,* **86,** 326–345.

Scorer, R. S., 1949: Theory of waves in the lee of mountains. *Quart. J. Roy. Meteor. Soc.,* **75,** 41–56.

Scott, M. J., L. W. Vail, C. O. Stockle, and A. Kemanian, 2004: Climate change and adaptation in irrigated agriculture: A case study of the Yakima River. *Proc. Universities Council on Water Resources Conf.,* Carbondale, IL, Southern Illinois University Carbondale, Paper 3.

Seager, R., N. Naik, M. Ting, M. A. Cane, N. Harnik, and Y. Kushnir, 2010: Adjustment of the atmospheric circulation to tropical Pacific SST anomalies: Variability of transient eddy propagation in the Pacific–North America sector. *Quart. J. Roy. Meteor. Soc.,* **136,** 277–296.

Selten, F. M., 2004: Tropical origins for recent and future Northern Hemisphere climate change. *Geophys. Res. Lett.,* **31,** L21205, doi:10.1029/2004GL020739.

Serreze, M. C., M. P. Clark, R. L. Armstrong, D. A. McGinnis, and R. S. Pulwarty, 1999: Characteristics of the western United States snowpack from snowpack telemetry (SNOTEL) data. *Water Resour. Res.,* **35,** 2145–2160.

Shutts, G., 1995: Gravity-wave drag parametrization over complex terrain: The effect of critical-level absorption in directional wind-shear. *Quart. J. Roy. Meteor. Soc.,* **121,** 1005–1021.

——, 1998: Stationary gravity-wave structure in flows with directional wind shear. *Quart. J. Roy. Meteor. Soc.,* **124,** 1421–1442.

Sinclair, M. R., D. S. Wratt, R. D. Henderson, and W. R. Gray, 1997: Factors affecting the distribution and spillover of precipitation in the Southern Alps of New Zealand—A case study. *J. Appl. Meteor.,* **36,** 428–442.

Smith, R. B., 1979: The influence of mountains on the atmosphere. *Advances in Geophysics,* Vol. 21, Academic Press, 87–230.

——, S. Skubis, J. D. Doyle, A. S. Broad, C. Kiemle, and H. Volkert, 2002: Mountain waves over Mont Blanc: Influence of a stagnant boundary layer. *J. Atmos. Sci.,* **59,** 2073–2092.

Smoliak, B. V., J. M. Wallace, M. T. Stoelinga, and T. P. Mitchell, 2010: Application of partial least squares regression to the diagnosis of year-to-year variations in Pacific Northwest snowpack and Atlantic hurricanes. *Geophys. Res. Lett.,* **37,** L03801, doi:10.1029/2009GL041478.

Stevenson, S., B. Fox-Kemper, M. Jochum, R. Neale, C. Deser, and G. Meehl, 2012: Will there be a significant change to El Niño in the twenty-first century? *J. Climate,* **25,** 2129–2145.

Stoelinga, M. T., M. D. Albright, and C. F. Mass, 2010: A new look at snowpack trends in the Cascade Mountains. *J. Climate,* **23,** 2473–2491.

Underwood, S. J., M. L. Kaplan, and K. C. King, 2009: The role of upstream midtropospheric circulations in the Sierra Nevada enabling leeside (spillover) precipitation. Part I: A synoptic-scale analysis of spillover precipitation and flooding in a leeside basin. *J. Hydrometeor.,* **10,** 1309–1326.

van den Dool, H. M., 2007: *Empirical Methods in Short-Term Climate Prediction.* Oxford University Press, 240 pp.

van Loon, H., and J. C. Rogers, 1981: The Southern Oscillation. Part II: Associations with changes in the middle troposphere in the northern winter. *Mon. Wea. Rev.,* **109,** 1163–1168.

Wright, C. S., and J. K. Agee, 2004: Fire and vegetation history in the eastern Cascade Mountains, Washington. *Ecol. Appl.,* **14,** 443–459.

Yarnal, B., and H. F. Diaz, 1986: Relationships between extremes of the Southern Oscillation and the winter climate of the Anglo-American Pacific coast. *Int. J. Climatol.,* **6,** 197–219.

Yin, J. H., 2005: A consistent poleward shift of the storm tracks in simulations of 21st century climate. *Geophys. Res. Lett.,* **32,** L18701, doi:10.1029/2005GL023684.

Zhang, Y., Y. Qian, V. Dulière, E. P. Salathé, and L. R. Leung, 2011: ENSO anomalies over the western United States: Present and future patterns in regional climate simulations. *Climatic Change,* **110,** 315–346.